Effects of heat treatment and build orientation on the evolution of ϵ and α' martensite and strength during compressive loading of additively manufactured 304L stainless steel

Nicholas C. Ferreri^{a,b}, Reeju Pokharel^{a,*}, Veronica Livescu^a, Donald W. Brown^a, Marko Knezevic^b, Jun-Sang Park^c, Michael A. Torrez^a, George T. Gray III^a

^aMaterials Science and Technology Division, Los Alamos National Laboratory, Los Alamos, NM 87544, USA

^bDepartment of Mechanical Engineering, University of New Hampshire, Durham, NH 03824, USA

^cAdvanced Photon Source, Argonne National Laboratory, Lemont, IL 60439, USA

Abstract

The effect of heat-treatment and build orientation on martensitic phase transformation in additively manufactured (AM) 304L stainless steel is studied and compared with conventionally produced wrought material. The relationships between observed martensitic transformations and material microstructures and their effects on mechanical strength are established through experimental observations. In situ high-energy X-ray powder diffraction measurements were performed to monitor the evolution of ϵ and α' martensite during compressive loading of stainless steel. Electron backscatter diffraction (EBSD) was used to provide insight on initial grain morphology, crystallographic misorientation within grains, and crystallographic texture. Heat

Email address: reeju@lanl.gov (Reeju Pokharel)

^{*}Corresponding author.

treatment alters the microstructure of AM samples creating different initial conditions. This difference in starting microstructure resulted in variability in martensitic transformation during compressive deformation. The rate of martensitic transformation decreased for samples treated with temperatures up to 1100°C, after which the AM microstructures recrystallized, resulting in increased rate of martensitic transformation for those samples treated at higher temperatures. It was also observed that aligning the axis of compression with the AM build direction resulted in a lower rate of strain-induced martensite formation as opposed to aligning the compression axis perpendicular to it. More favorable distribution of crystal orientations in the latter loading orientation promoted martensitic transformation. These and additional experimental observations from EBSD in terms of kernel average misorientation, mean grain orientation spread, and mean crystallite size reveal strong microstructural effects on strength of additively manufactured metallic materials.

Keywords:

martensite, plastic deformation, additive manufacturing, 304L stainless steel, in situ high-energy X-ray diffraction

1. Introduction

- Austenitic stainless steels are a large family of alloys with wide-ranging
- a applications due to their high corrosion resistance, high mechanical strength
- 4 over a large range of temperatures, high ductility and formability, and ex-
- 5 ceptional weldability [1, 2]. Some of these steels are metastable at room
- 6 temperature and will undergo solid-state phase transformations if plastically

strained, which can greatly increase material strength and formability. The transformations observed in these steels are from the initial face-centered cubic (fcc) austenite (γ) directly to a body-centered tetragonal (bct) martensite (α') or from γ to α' through an intermediate hexagonal close-packed (hcp) martensite (ϵ) [3, 4]. These transformations are shown in equations 1 and 2.

$$\gamma \to \alpha'$$
 (1)

$$\gamma \to \epsilon \to \alpha'$$
 (2)

Martensitic transformations in steels occur spontaneously upon cooling 12 to temperatures below the critical martensite start temperature M_s ; however, with the aid of plastic strain, these transformations can be induced at temperatures above M_s , up to a critical temperature M_d at which point the austenite becomes thermodynamically stable in the presence of plasticity [2]. Martensite formed during plastic deformation occurs via an athermal, diffusionless shear transformation and is commonly referred to as mechanically-induced martensite [1]. At low plastic strains, strain-induced martensite transforms according to Eq. 2; however, at high plastic strains when the hcp phase has been depleted, but martenite will transform directly from the fcc austenite [2, 4, 5]. This understanding is based on observations of ϵ martensite in low carbon steels at low plastic strains, but not at high strains even when α' martensite continues to transform [2, 4]. ϵ martensite nucleation occurs when partial dislocations separate beyond some critical distance and the faulted hcp zone within the austenite matrix becomes thermodynamically stable [3]. This transformation is thought to occur when shear bands containing a high stacking fault density intersect other slip bands, grain boundaries, or twin boundaries [2, 5, 6, 7]. At higher levels of plastic strain, α' martensite has

been observed to transform directly from austenite in low carbon steels from dislocation pileups on $\{111\}\gamma$ planes [8] and at shear band intersections [9]. Factors that influence austenite stability are chemical composition (alloying additions) and temperature, and factors that affect the extent and rate of strain-induced transformations are strain rate, stress state, grain size, grain orientation, stacking fault energy (SFE), and degree of plastic strain [2, 3, 10]. Mechanically-induced martensite has been observed to form under applied stresses in metastable stainless steels such as 304L and increases mechanical strength due to the high strength of martensite.

Multiple studies have observed the evolution of strain-induced marten-39 site in uniaxially loaded 304L stainless steel [3, 11, 12, 13], but the extent to which of these transformations occur in additively manufactured (AM) 304L stainless steel (SS) at room temperature remains poorly quantified. AM is a rapidly developing processing pathway due to its ability to produce end-use parts with complex geometries that would otherwise be impossible or very expensive and time consuming to make with traditionally cast or wrought alloys [14]. Despite the weld-like microstructures commonly seen in AM materials, the quasi-static mechanical properties of these alloys often compare favorably to their cast or wrought counterparts [15, 16]. As a result, considerable research is being conducted to establish empirical connections between AM processing parameters, microstructure, phase composition, and their mechanical properties [15, 16, 17, 18, 19, 20, 21, 22]. The current work focuses on understanding how different initial microstructures produced by AM and subsequent heat treatments affect quasi-static mechanical properties with respect to martensite transformations during deformation in a 304L-SS

fabricated via laser powder bed fusion.

Over the past two decades, in situ high-energy X-ray diffraction tech-56 niques to monitor microstructural evolution in materials during deformation have been widely used [23, 24, 25]. In particular, the ability to accurately model Bragg peak intensity and breadth through crystallographic texture, crystallite/grain size, and lattice parameter gradient (microstrain) measurements in low weight fraction phases during deformation has enabled the in situ quantification of material phase composition. In this study, in situ highenergy X-ray powder diffraction measurements were performed to monitor the phase transformation in AM-304L-SS as a function of imposed macroscopic compressive strain. Compression samples were fabricated from one of two regions in a plate of this steel, and with one of two orientations with respect to the AM build direction. The intent was to test for mechanical heterogeneity and anisotropy, respectively, and see if there was significant influence on martensite evolution. Moreover, samples were heat treated to observe the effect of different initial microstructures on martensite evolution. Electron backscatter diffraction (EBSD) images of samples pre and post deformation were taken to measure local crystallographic misorientations to quantify crystallographic recovery and static recrystallization. The results are also intended to direct future model development of strain-induced phase transformations in 304L-SS. Combining polycrystal plasticity modeling with experimental datasets containing a materials phase evolution during deformation can offer profound insight into the deformation micro-mechanics of the observed system [16, 26, 27, 28, 29, 30].

2. Materials and methods

2.1. Sample preparation

103

Detailed descriptions of the additive manufacturing of the AISI 304L grade SS studied here and the baseline wrought materials are reported elsewhere [31, 32, 33, 34], and only a brief description of the AM build process will be given here. An AM-304L-SS plate $(86 \times 50 \times 10 \text{ mm}^3)$ was deposited using the laser powder bed fusion (LPBF) method with the starting powder size ranging between 15-45 μ m. The LPBF processing parameters used were the Electro Optical Systems (EOS M290) [35] developed PH-1 20 μ m settings and the build pattern comprised of layers deposited at 67 degrees from each other. The initial state characterization of these materials is also reported elsewhere [32, 34].

Schematics of the AM-304L-SS plate, locations, and orientations of the compression specimens are shown in Fig. 1(a). All AM samples used in this study were obtained from one of two excised blocks (B2 and B7) that originated from the top and bottom of the as-built AM plate (this varied block height above the substrate) and is indicated in Figure 1(a). A set of compression samples with dimensions 2 mm × 1.9 mm (sides) × 4 mm (height) were fabricated from the steel plate using electro-discharge machining (EDM). The specimens were machined such that their loading axis aligned with either the build direction (BD) or the through-thickness direction (TD). The wrought compression sample had an identical geometry as the AM samples, where the loading axis (the elongated axis) parallel to the rolling direction is referred to as the axial direction, and the other two axes are in-plane (IP) axes.

In situ compression samples obtained from two separate regions of the

AM-304L-SS plate were used to test for material heterogeneity and mechanical uniformity. Samples originated from the same region of the AM plate, 105 but with different loading axes with respect to the AM build direction were used to test the influence of texture on martensite evolution and mechanical 107 anisotropy. To study the effect of microstructure on martensitic transforma-108 tion, AM samples originated from the same region of the AM plate and with 109 identical loading axes with respect to the AM build frame were heat-treated 110 at different temperatures. Prior to loading, these samples underwent one of 111 several heat treatments. Each sample was heated in an argon atmosphere to 112 either 850°C, 950°C, 1000°C, 1100°C, 1200°C, or 1300°C and held for 1 hour 113 at temperature and then air cooled. The post-processing heat-treatment 114 created samples with varying microstructures and therefore different initial 115 conditions for compression.

17 2.2. In situ high-energy X-ray diffraction during compressive loading

The schematic of the experimental setup is shown in Fig. 1(b). In situ 118 high-energy X-ray powder diffraction experiment was performed at the Advanced Photon Source (APS) 1-ID-E beamline. The X-ray energy was 80.725 keV (wavelength of 0.015359 nm), the sample to detector distance was ap-121 proximately 650 mm, and the size of the incident beam was 0.1 mm \times 0.1 122 mm. The instrument was calibrated using a standard CeO₂ specimen [36]. 123 Two-dimensional WAXS patterns were converted into intensity vs. d-spacing using GSAS-II [37]. Monotonic, displacement-controlled compression tests 125 were carried out at room temperature at a strain rate of $4x10^{-4}$ s⁻¹ using an 126 MTS servo-hydraulic load frame. The wide angle X-ray scattering (WAXS) 127 data were collected on a single panel silicon-based integrating area detector

[38]. Both the WAXS and the MTS load frame data acquisition rates were set to 10 Hz, making it possible to obtain WAXS data as a function of sample displacement.

2.3. Microstructural characterization

Samples were prepared for scanning electron microscopy by grinding with 133 silicon carbide (SiC) abrasive paper, beginning with medium grits and ending with fine grit. Subsequent mechanical polishing took place using a 5:1 by 135 volume mixture of an aqueous 0.3 μ m alpha alumina (Al₂O₃) suspension and 136 concentrated hydrogen peroxide (H₂O₂). Mechanical preparations concluded 137 with a final polish of a 5:1 by volume mixture of an aqueous $0.04 \mu m$ colloidal 138 silica (SiO₂) suspension and concentrated H₂O₂. Just prior to characterization, samples were cleaned and coated with a carbon-based conductive paint. EBSD patterns were collected using a ThermoFisher Scientific TM Apreo scan-141 ning electron microscope (SEM) with an accelerating voltage of 20 kV and step size of 0.75 μ m. Scan area was 500 x 500 μ m² per sample and provided information on crystallographic texture and grain morphology in the as-built and heat-treated material for both initial and deformed specimens. 145

EBSD was performed on all samples to collect crystallographic orientation data from which sample microstructures were reconstructed and image
quality (IQ), kernel average misorientation (KAM), grain orientation spread
(GOS), and crystallite size information were calculated. EBSD data was analyzed using the EDAX TSL Orientation Imaging Microscopy (OIM) Analysis software in addition to the MTEX [39] toolkit in MATLAB. EBSD data
with a confidence index (CI) less than 0.1 was discarded due to those values
being associated with low orientation indexing accuracy [40]. Additionally,

a grain and a crystallite are defined as a group of 5 or more pixels with less than 5° and 0.75° of crystallographic misorientation with each other, respectively. This definition incorporates both sub-grains and grains while preventing unintentional crystallite classification that could result from intragranular orientation gradients, indexing errors, etc. Crystallites bordering the edge of the EBSD scans were not incorporated into crystallite size calculations. Pole figures were also constructed from EBSD data, but it should be noted that scans of the AM samples heated at 1200°C and 1300°C, as well as the wrought sample, were not reported because the mapped area did not include enough grains for statistically relevant pole figure calculations.

64 2.4. X-ray data analysis

A step-by-step guide to the phase analysis performed in GSAS-II us-165 ing in situ X-ray diffraction data is provided in Appendix A, and only a brief description of the procedure exists here. In order to determine the lattice parameters, microstrain (lattice parameter gradient contributing to peak broadening), and crystallographic texture (12^{th} order spherical harmonics) for the γ phase in each sample, a series of Rietveld refinements was performed on the deformed X-ray diffraction datasets. This was not done 171 for ϵ and α' phases because all deformed AM-304L-SS datasets had low in-172 tensity peaks corresponding to the martensite phases, which were difficult to fit robustly during Rietveld analysis [41]. The deformed wrought material, however, had higher intensity peaks corresponding to the martensite phase; therefore, microstructural parameters for the martensite phase were 176 determined by refining the deformed wrought 304L-SS dataset, which were 177 then applied to all other datasets. Mean crystallite/grain sizes were also determined through refinement of the deformed wrought dataset for ϵ , and α' while γ crystallite/grain sizes were measured in each sample via EBSD. Subsequent sequential Rietveld refinements were performed for each $in\ situ$ test where the diffraction histogram corresponding to each X-ray exposure was fit, sequentially, in GSAS-II. These refinements incorporated γ , ϵ , and α' phases and calculated phase weight fractions for each histogram. The martensite and austenite lattice parameters and crystallite sizes (also martensite microstrain) were fixed for each phase during the sequential refinements, while γ microstrain, γ hydrostatic strain (to account for any net change in lattice parameter during deformation), γ texture, and phase fractions were refined.

Atomic displacement parameters, (often referred to as Debye-Waller factors or B_{iso}) which describe the attenuation of X-ray scattering caused by thermal atomic motion, were based on values calculated by Peng et. al in [42] and fixed in all refinements. This assumes that the crystallite sizes and atomic displacement parameters for each martensite phase are identical across all samples and do not evolve under macroscopic elastic or plastic strains. This is a reasonable assumption for undeformed martensite because the mechanisms causing it to transform produce crystallites with a specific morphology [7]. Additionally, dynamic recrystallization, which would alter crystallite size, is unlikely in any phase because mechanical tests were only carried out to small total plastic strains. Refining crystallite size is also unnecessary because small changes in value would have a negligible effect on peak breadth given the length scale of crystallites in the material. B_{iso} will rise with increased elastic strain [43], but was not refined because slight changes in its value would also have little effect on peak intensities at high

d-spacings. Moreover, because the martensite phases have low-intensity or absent peaks at low plastic strains, which are difficult to fit, simultaneously refining B_{iso} , crystallite size, microstrain, and texture would not have resulted in converged values [41]. Profile fitting uncertainty is calculated during each refinement in GSAS-II and is reported with phase weight fractions. These values are large for the 1200°C and 1300°C sample datasets due to large grain size, which resulted in under-sampled, suboptimal diffraction patterns with low signal/noise that were difficult to fit using the Rietveld method. These two datasets were plotted using moving averages because of the high degree of noise.

214 3. Results

3.1. Mechanical Response

Macroscopic true stress versus true strain curves for specimens loaded 216 under uniaxial compression are shown in Fig. 2. Tests were performed until 217 samples reached a maximum true strain of approximately 11%. Fig. 2(a) 218 shows compression curves that correspond to samples originating from blocks 219 B2 and B7 both with their loading axes oriented along BD. Both samples exhibit yield strengths (YS) of about 450 MPa and nearly identical flow stresses. This was also seen in a study by Wang et al. who observed similar yield and ultimate tensile strengths for BD and TD samples in AM-304L-223 SS produced by directed energy deposition (DED) [20]. The compression curve corresponding to a sample originating from block B2, but with its loading axis along the through-thickness axis (TD) is also shown. Although this sample shares a YS with the former two (~ 200 MPa greater than the

wrought material), it has a smaller hardening rate resulting in a lower flow stress, which begins to manifest around 5% true strain. However, because these curves each represent a single *in situ* test, it is likely this flow stress discrepancy is statistical scatter.

Fig. 2(b) shows the macroscopic true stress-strain responses during com-232 pressive loading of AM samples that were subjected to different HTs prior to 233 testing. The compression samples were all cut in the same orientation with 234 respect to the AM build frame (BD parallel to loading). All HT samples had lower YS and flow stress than the as-built AM-304L-SS. The highest YS of the HT samples (approximately 375 MPa) corresponds to the sample 237 held at the lowest temperature during HT (850°C), and the lowest YS (\sim 125 MPa) corresponds to the sample held at the highest temperature (1300°C). Moreover, increasing or decreasing the HT soak temperature by 100-150°C resulted in a respective drop or gain in YS by ~ 50 MPa. The one exception is the nearly 150 MPa difference in YS between the AM-304L-SS heated at 1100°C and 1200°C. Also of note is that the wrought material had a YS (250 MPa) between that of the AM samples HT at 1100°C (300 MPa) and 1200°C (150 MPa). Concerning flow stress, the hardening rate of the 850°C sample is like that of the as-built material, but samples heated at or above 950°C had slightly higher hardening rates, which were more similar to that of the wrought material. 248

3.2. Phase evolution

Fig. 3 shows X-ray diffraction profile corresponding to a single exposure, both prior to loading and at a compressive strain of 11% for *in situ* tests performed on wrought, as-built AM, and HT AM 304L samples. The profile

corresponding to the undeformed material show no evidence of martensite in the initial state (true strain = 0%), apart from the wrought material, which 254 displays low-intensity α' reflections. However, profile in Fig. 3 (true strain 255 = 11%), which corresponds to the deformed material, display both ϵ and α' reflections for all tested samples with the greatest ϵ and α' peak intensities 257 being in the wrought data. This observation in PBF 304L-SS is different 258 from studies by Brown et al. [31] and Wang et al. [20], where strain-induced 259 martensite was not observed in deformed DED 304L-SS. Two-dimensional Xray diffraction patterns for the deformed wrought and AM as-built material 261 are also provided in Appendix B, which clearly shows continuous intensity 262 contributions from both austenite and martensite phases present in the de-263 formed steels. 264

The martensite evolution during the *in situ* testing of as-built samples 265 manufactured from different blocks with varied loading axis orientations (B7-266 BD, B2-BD, B2-TD) are shown in Fig. 4. The initial and final phase weight 267 percentages are shown in Table 1. All as-built samples began in situ testing 268 with no detectable ϵ or α' martensite, whereas the wrought sample had no 269 detectable ϵ martensite, but consisted of 0.26 wt. % α' martensite. Similar to the true stress-strain response, there is negligible difference in material behavior between the two BD samples cut from the same block; both have indistinguishable discrete ϵ and α' martensite volume percentages, relative 273 to their respective uncertainties, during loading. The sample from block B2 with loading axis along TD, however, evolved more ϵ and α' martensite at 11% applied macroscopic strain than the sample from block B2 with loading axis along BD. The former had final ϵ and α' weight percentages of 4.21%

and 1.26%, whereas the latter had 5.44 % and 1.95 %, respectively. The wrought material had ϵ and α ' martensite weight percentages of 7.01% and 2.80%, respectively, at 11% applied macroscopic strain.

Since B2 and B7 samples showed close to identical macroscopic load-281 ing and martensitic transformation behaviors, only heat-treated samples ob-282 tained from the B2 block were used for in-situ compressive loading measure-283 ments. Fig. 5 shows martensite evolution as a function of strain for HT AM 284 samples that underwent in situ testing. The initial and final phase weight 285 percentages of the martensite phases are shown in Table 2. Similar to previous tests, no martensite was detected in undeformed AM material. Weight 287 percentages of ϵ and α' at 11% applied macroscopic strain were 2.87% and 288 0.45% in the AM sample heated to 850°C and final ϵ quantity was similar in 289 the deformed 950°C sample while α' was slightly lower. The 1100°C sample had the lowest weight percentages of final ϵ and α' martensite at 2.00% and 291 0.23\%, respectively. The 1200°C sample, however, at 11\% applied macro-292 scopic strain had increased levels of α' almost to that of the as-built sample and increased levels of ϵ to similar levels as the 850°C and 950°C samples. 294 The 1300°C sample had an even higher weight percent of α' (5.83%), which was between that of the as-built and wrought samples at 11% applied macroscopic strain.

²⁹⁸ 4. Discussion

299 4.1. Effect of crystallographic recovery on martensite evolution

A qualitative microstructural analysis with emphasis on KAM, austenite GOS, and austenite crystallite size was performed on undeformed samples

to provide insight into the extent to which crystallographic recovery and recrystallization occurred in the undeformed 304L samples during HT. This 303 allowed for correlations amongst recovery, recrystallization, and martensite evolution to be made. High KAM often highlights the presence of dislocation structures within grains [44], which form when materials with relatively 306 high dislocation content and high SFE undergo a period of crystallographic 307 recovery. During recovery, dislocations rearrange themselves to reduce total 308 lattice energy by creating slightly misoriented sub-grains [45]. Therefore, a decrease in crystallite size will also be an indicator of recovery. 310

Mean KAM and mean crystallite size measurements are shown in Table 3 while low angle ($<5^{\circ}$ misorientation) sub-grain boundaries are overlaid in 312 red on GOS maps in Fig. 6 for all undeformed samples. Mean crystallite 313 sizes were 23.51 μ m and 16.13 μ m for the as-built and 1000°C AM samples, while mean KAM values were 0.563° and 0.738°, respectively. This increase in mean KAM and decrease in mean crystallite size, combined with an observed increase in sub-grain boundaries as seen in Fig. 6, is strong evidence of crystallographic recovery occurring as a result of heat-treatment. 318

311

315

316

317

It has been reported that the decrease in crystallite size as a result of 319 recovery would decrease the chance of shear band formation and would lower stacking fault probability [46] and would therefore reduce strain-induced 321 martensite nucleation [2, 47, 48]. This was observed during in situ compres-322 sion. Martensite transformation rates were high in the as-built sample, lower in the 850°C and 950°C AM samples, and lowest in the 1100°C AM sample (see Fig. 5). Note that the sample heated at 1000°C was not measured during in situ loading experiment at the beamline but was used for EBSD measurements, due to lack of samples heat treated at 850°C and 950°C. The AM sample heated at 1100°C had lower mean KAM (0.630°) and greater mean crystallite size (20.97 μ m) than the AM sample heated at 1000°C because it had begun to recrystallize.

331 4.2. Effect of recrystallization on martensite evolution

Both ϵ and α' martensite began transforming at lower plastic strains and 332 at higher rates in the wrought sample than any AM sample, as seen in Fig. 5. Moreover, strain-induced martensite began transforming at higher plastic strains and at slower rates with increased HT temperature until 1200°C when rates began rising again. This rise is coincident with the recrystallization of the AM microstructure in samples heated to 1200°C and 1300°C. Recrystallization is evident due to the decrease in mean GOS, which is shown in Table 3. GOS is a measure of the range of crystallographic orientations 339 within a grain and often highlights the presence of recrystallized grains [48]. Mean GOS values remain high for as-built, 1000°C, and 1100°C samples, but drop significantly for 1200°C and 1300°C specimens. Newly recrystallized grains are strain-free with little-to-no orientation gradient, have low dislocation content, and if given sufficient time at elevated temperatures can 344 coarsen significantly. Such grains are seen in Fig. 6 with dark blue coloring, 345 corresponding to a low GOS. Due to the presence of strain-free grains and lack of sub-grain dislocation structures, it is clear the 1200°C and 1300°C microstructures fully recrystallized while the 1100°C microstructure did so partially. This also explains the slight drop in mean KAM and GOS between 1000°C and 1100°C and the large drop between 1100°C and 1200°C. More-350 over, it explains the slight increase in mean crystallite size between 1000°C and 1100°C and the large increase between 1100°C and 1200°C. Because an increase in austenite crystallite size increases the probability of strain-induced martensite nucleation (due to increased chance of shear band and stacking faults formation) [2, 46, 47], we see an increase in the rate of martensite transformation during loading in recrystallized microstructures.

Concerning the wrought material, martensite transformation rate is higher than the non-recrystallized AM samples primarily due to having a much larger mean crystallite size. The difference in martensite evolution between recrystallized AM material and the wrought sample is also likely in part due to a larger wrought crystallite size; however, differences in crystallographic texture and solute homogeneity between AM and wrought material may also play a role.

4.3. Effect of crystallographic texture on martensite evolution and mechanical strength

As-built AM samples originating from the same block (B2) of material 366 were machined with their loading axes parallel to the build (BD) and transverse (TD) directions. It was found that while both samples exhibited sim-368 ilar YS, the flow stress was slightly higher in the TD sample at true strains 369 >5%. Additionally, both ϵ and α' martensite transformed at higher rates 370 and resulted in larger final weight percentages in the TD sample versus the 371 BD sample. The orientation relationship between austenite and incipient martensite adjacent lattices is $\{111\}\gamma \parallel \{0001\}\epsilon$ for γ and ϵ crystals and 373 $\{001\}\gamma \parallel \{001\}\alpha'$ for γ and α' crystals [13, 49]. Additionally, the orientation 374 relationship between ϵ and incipient α' crystals is $\{0001\}\epsilon \parallel \{110\}\alpha' [50]$. 375 This implies that if the austenite has a bulk crystallographic texture, then

so would the transformed martensite. Inverse pole figures showing α ' and ϵ martensite texture calculated from X-ray diffraction patterns (post-loading) are shown in Appendix C. Moreover, it has been reported in other works [11, 30, 45] that while under compressive load, the γ to α' transformation via intermediate ϵ stacking faults is facilitated in 304L-SS when austenite grains are oriented with 001γ plane-normal to the axis of loading. This is made possible due to the crystallographic orientation relationships amongst these phases [13, 50, 51].

As seen in Fig. 7, the pole figures constructed from EBSD data of the 385 undeformed as-built, 1000°C, and 1100°C AM material have a $\{110\}\gamma$ fiber, 386 but virtually no $\{001\}\gamma$ texture components parallel to BD. This is indicated 387 by the spike in pole density, represented as multiples of random distribution 388 (m.r.d.), in the center of the as-built $\{110\}\gamma$ pole figure and the low pole densities in the centers of the as-built $\{001\}\gamma$ pole figures. $\{110\}\gamma$ fibers 390 have been observed before in AM-304L-SS [16]. Additionally, 90° from BD 391 (in all directions) in the $\{001\}\gamma$ pole figures is a ring component. This ring 392 has a lower associated m.r.d. than the $\{110\}\gamma$ fiber along BD, but it does 393 indicate some degree of preferred orientation where $\{001\}\gamma$ poles are along TD. This preferred orientation can also be seen in the undeformed austenite inverse pole figures in Appendix C. Therefore, due to the lack of grains with 396 $\{100\}\gamma$ poles oriented along BD, as indicated by the ~ 0 m.r.d., and the relatively high presence of grains (2 to 3 m.r.d.) with $\{100\}\gamma$ poles oriented along TD, it is reasonable to conclude that the as-built TD sample evolved more martensite than the BD sample during compressive loading due to initial crystallographic texture. More precisely, the alignment of TD with the

loading axis was favorable, with respect to the crystallographic texture of the AM-304L-SS, and resulted in higher quantities of strain-induced martensite during deformation as described by Eq. 2.

4.4. Effect of martensite evolution and heat-treatments on mechanical strength

The effect martensite transformations had on the flow stress observed in 406 samples is seen to be minimal if at all. YS decreases continually in AM samples with increasing HT temperature, similar to flow stress, and is unaffected 408 by strain-induced martensite transformations, which occur after the onset of 409 plasticity. This was also observed in a study by Brown et al. [31] who posited that the decreases in the strength of a HT AM-304L-SS fabricated via DED 411 were due to decreases in dislocation density resulting from heat treating at higher temperatures. Brown et al. [31] also observed a significant drop in the strength of AM-304L-SS heated above 1100°C, where the as-built AM grain 414 morphology transformed into an equiaxed structure after recrystallization, 415 similar to what was observed in this work [31]. Crystallographic recovery reduces the dislocation content in a material by mobilizing dislocations, which annihilate at matrix defects and minimize lattice energy [52]. Recrystallization implies nucleation and growth of low dislocation density grains, which 419 if grains become coarse will also contribute to softening according to the 420 Hall-Petch relation [52, 53]. Therefore, the steady decline in YS observed 421 at HT below 1100°C is due to crystallographic recovery, while static recrystallization is responsible for the drop in strength observed in AM-304L-SS 423 heated above 1100°C. The wrought material has a YS (~ 250 MPa) between that of the 1100°C and 1200°C sample likely because of a combination of its large grain size and high dislocation content, relative to the recrystallized

AM samples. Similar YS for wrought 304-SS were also observed in studies by Brown et al.[31] and Gray III et al.[32].

4.5. Effect of material heterogeneity on martensite evolution and mechanical strength430

As-built samples oriented identically with respect to the compression 431 frame (BD along loading axis) were machined from blocks B2 and B7 within a single AM plate. It was found that both samples exhibited near identical 433 true stress-strain responses and phase evolution when loaded in compression. 434 The thermal profile of the as-built plate varied as a function of distance from 435 the build plate during cyclic heating [16, 31, 54]. Typically, material near the build plate cools more rapidly during solidification than further from the built plate. Mechanical uniformity, however, was confirmed due to the similar performance and phase evolution in BD samples originating from the block 439 closest (B2) and farthest from the build plate (B7). Although AM material has localized heterogeneity, at length scales corresponding to sample size the plate material was either homogenous or the heterogeneities did not affect mechanical performance over the range of tests conducted in this work. 443

On sub-grain length scales, it is likely that there was chemical hetero-444 geneity in the as-built AM material in the form of solute micro-segregation 445 resulting from cellular and/or dendritic solidification where solute atoms concentrated in cell walls or dendrite interfaces [52]. In micro-segregated 304L-SS, solute-poor cell/dendrite cores would have higher SFE due to the absence of SFE-lowering elements such as Cr, Si, and Mn, which would have decreased the probability of strain-induced martensite nucleation [55]. Therefore, it is possible that the 1 hour soak time during the AM heat-treatments

446

was not long enough for significant solute diffusion to take place at temperatures lower than 1300°C HT, which resulted in unchanged, chemically inhomogeneous materials. This potential for solute diffusion along concentration gradients in the 1300°C material could explain the observed increase in martensite transformation rate.

5. Conclusions

466

467

468

469

470

471

472

473

474

This work has examined the effect of sample build orientation and heattreatment on the evolution of martensite and strength in an AM-304L-SS
alloy. In situ high-energy X-ray diffraction was performed during compressive
loading to examine martensite evolution as a function of macroscopic strain.
Macroscopic stress-strain response was also recorded during in situ tests and
EBSD was used to provide insight on austenite grain/crystallite morphology,
intragranular crystallographic misorientation, and crystallographic texture.
The main conclusions of this study are:

- Static recrystallization of an AM-304L-SS microstructure as a result of heat-treatment increases the rate at which strain-induced martensite transforms during compressive loading. This is primarily due to an increase in mean austenite crystallite size, with respect to the initial microstructure, and facilitates martensite transformation by means of increasing the probability of shear band and stacking fault formation, which raises the number of potential martensite nucleation sites.
- Crystallographic recovery in an AM-304L-SS microstructure as a result of heat-treatment decreases the rate at which strain-induced martensite

transforms during compressive loading. This is due to the formation of low-angle, intragranular dislocation structures during a period of recovery that reduce mean austenite crystallite size. This hinders martensite transformation by reducing probability of shear band and stacking fault formation, which decreases the number of potential martensite nucleation sites.

475

476

477

478

479

480

481

482

483

485

486

487

488

489

491

493

494

495

497

498

- Crystallographic texture influenced the rate at which strain-induced martensite formed in as-built AM-304L-SS. Samples with loading axis parallel to BD had lower final weight percentages of martensite than samples with loading axis parallel to TD. This was due to the lack of grains with $\{100\}\gamma$ pole oriented along BD and the relatively high presence of grains with $\{100\}\gamma$ pole oriented along TD.
- Phase composition had no appreciable effect on the flow stress of AM (as-built and heat-treated) and wrought 304L stainless steel. YS decreased for AM samples as HT temperature increased, which was caused by crystallographic recovery below 1100°C and recrystallization above 1100°C.
- At length scales corresponding to compression sample size, the AM-492 304L-SS plate was either homogenous or the heterogeneities did not affect mechanical performance over the range of tests conducted in this work. It is, however, plausible that on sub-grain length scales, solute heterogeneity created localized regions within the austenite matrix that had high SFE, which lowered the probability of shear banding and consequently strain-induced martensite nucleation.

The current work will be complemented with modeling in the future.

Complementary neutron diffraction measurements will be used to extract
the initial bulk textures for crystal plasticity model instantiation. Along
with the martensite phase evolution information, additional analysis of the
in situ X-ray data will be performed to extract hkl reflection specific lattice
strain evolution during compression and will be used for model validation.

505 Acknowledgements

This work was supported by the US Department of Energy through the Los Alamos National Laboratory. Los Alamos National Laboratory is oper-507 ated by Triad National Security, LLC, for the National Nuclear Security Ad-508 ministration of U.S Department of Energy (Contract No. 89233218CNA000001). 509 Specifically, NCF, RP, DWB, MAT and GTG acknowledge funding from the Science Campaign 2 program at LANL. M.K. would like to acknowledge the support provided by the U.S. National Science Foundation under the Grant 512 No. OIA-1757371. This research used resources of the Advanced Photon 513 Source, a Department of Energy (DOE) Office of Science User Facility operated for the DOE Office of Science by Argonne National Laboratory Contract DE-AC02-06CH11357. Experimental support from T. J. Stockman (LANL) and the staffs of the APS-1-ID-E beamline are also acknowledged.

Appendix A

519

Phase analysis procedure performed in GSAS-II:

- I) CeO_2 calibration
- 1. Import summed two-dimensional (2D) CeO2 data (diffraction pattern) files.
- 2. Calibrate \rightarrow Integrate 2D data (full integration) \rightarrow 1D \rightarrow Full Rietveld with CeO₂
- 3. Save sample, instrument, and image control parameters.
- 526 II) 304L 2D data integration
- 1. Import summed 2D data files.
- 2. Load CeO_2 image control parameters \rightarrow Integrate 2D data (full integration) \rightarrow one dimensional (1D) histograms.
- 3. Save 1D data.
- 531 III) Martensite phase calibration
- 1. Import γ , ϵ , and α' .cif files and last 1D dataset (highest strain with most martensite).
- 2. Set Biso values for all phases based on the literature.
- 3. Set γ crystallite sizes based on EBSD measurements.
- 4. Import instrument and sample parameters.
- 537 5. Refine hist scale, background (bk), weight fractions (VF), γ lattice constants, γ crystallite size, γ microstrain.
- 6. Refine hist scale, bk, WF, γ lattice constant, γ microstrain, sample X + Y coordinates.
- 7. Refine hist scale, bk, WF, γ lattice constant, γ microstrain.
- 8. Refine hist scale, bk, WF, ϵ lattice constants.

- 9. Refine hist scale, bk, WF, ϵ lattice constants, ϵ microstrain.
- 10. Refine hist scale, bk, WF, ϵ lattice constants, ϵ microstrain, ϵ crystallite size.
- 11. Refine hist scale, bk, WF, ϵ texture (spherical harmonics=12).
- 12. Refine hist scale, bk, WF, α' lattice constants.
- 13. Refine hist scale, bk, WF, α' lattice constants, α' microstrain.
- 14. Refine hist scale, bk, WF, α' lattice constants, α' crystallite size.
- 15. Refine hist scale, bk, WF, α' texture (spherical harmonics=12).

551 IV) 304L 1D data refinement/analysis

555

556

566

- 1. Import Austenite and Martensite cif files and first steel 1D dataset.
- (a) Import sample and instrument parameter files from CeO₂ calibration.
 - (b) Add constraint that phase weight fractions sum to unity.
 - (c) Manually enter phase parameters that were determined in Step 3.
- (d) Locate the first histogram where ϵ peaks begin forming and manually fix ϵ WF to zero in all previous histograms. Repeat for α' .
- (e) Refine: bk, histogram scale parameter, γ lattice constant.
- (f) Refine: bk, histogram scale parameter, γ lattice constant, γ microstrain.
- (g) Refine: bk, histogram scale, γ microstrain, sample X + Y displacement.
- (h) Refine: bk, histogram scale, γ microstrain, γ texture (spherical harmonics = 12).
 - 2. Import the rest of the 1D datasets.

- (a) Perform sequential refinement on all profiles with freed parameters.
 - 3. Sequential refinements
- (a) Controls: SVD zero tolerance = 0.0001, Max cycles = 15, copy results to next histogram, begin at last histogram.
 - (b) Refine: histogram scale parameter, bk, VF, γ hydrostatic strain, γ microstrain.
 - (c) Refine: histogram scale, bk, VF, γ hydrostatic strain, γ microstrain, γ texture (spherical harmonics =12).
 - 4. Export sequential refinement phase information as csv.

$\mathbf{Appendix}\;\mathbf{B}$

569

572

573

574

575

576

Fig. 8 shows two-dimensional X-ray diffraction patterns for the deformed wrought and AM as-built material, where diffraction signals from both austenite and martensite phases are visible. Resolvable γ , α' , and ϵ Debye-rings are labeled at higher d-spacings (toward the center of the diffraction patterns), and all phases appear textured apparent through azimuthal variation in Debye-ring intensities. Note that the intensity scales are different for these diffraction patterns due to varying degree of attenuation used during data acquisition. The intensity scale has arbitrary unit.

586 Appendix C

Inverse pole figures (IPFs) for undeformed and deformed γ phase are shown in Fig. 9, and the deformed (IPFs) for the α ' and ϵ phases are shown in Fig. 10. From single 2D X-ray diffraction patterns collected before and/or

after loading for each sample, orientation distribution functions were calculated using the E-WIMV algorithm in the diffraction software Maud and 591 refined using the Rietveld method to model the texture of γ , α' , and ϵ phases. This procedure is explained in further detail in Wenk et al. [56]. No sample symmetry was assumed during the texture refinements and from the final orientation distribution functions, inverse pole figures were plotted. Because 595 no sample rotations were performed about the loading axis during experi-596 mentation, it is possible there were many grains in the sampled volume of material oriented such that they never met the Bragg criteria for diffraction and were therefore not included in texture calculations. This increases the likelihood of calculating an orientation distribution function that describes 600 non-physical texture components. That being said, the as-built austenite 601 inverse pole figures (undeformed samples) are in good agreement with the textures reported in [34]. Because of this, we assume the X-ray diffractionproduced textures to be reasonable approximations. Martensite textures are 604 not reported for undeformed samples because martensite was either not observed or had too few peaks (and of low intensity) to fit a texture model. Various 1200°C and 1300°C plots are missing because of low quality powder data, which made texture refinements infeasible.

AM process conditions create a {220} fiber-like texture in the as-built 609 state. This has been previously reported for AM-304L-SS, where the as-built 610 texture resembled that of the wrought 304L steel subject to compressive deformation [34]. Heat treatment does not evolve the initial γ texture, at least up to 1100°C, and the initial features are preserved. Compression of this austenite phase seems to align the {220} crystal planes with the loading

611

axis and also creates rings in the previously spotty diffraction patterns (as seen in 1200°C and 1300°C samples). We observe these features in the inverse pole figures, but only slightly, because the macroscopic true strain is small (\sim 11%). Because of small macroscopic strain levels, we do not see major γ texture evolution. α ' and ϵ textures are products of the strain-induced phase transformations.

References

- [1] J. M. Alves, L. P. Brandao, A. d. S. Paula, The influence of sample preparation on the quantitative analysis of the volume fraction of martensite formed in a 304l trip steel, Materials Research 18 (2015) 159–163.
- [2] J. A. Lichtenfeld, C. J. Van Tyne, M. C. Mataya, Effect of strain rate
 on stress-strain behavior of alloy 309 and 304l austenitic stainless steel,
 Metallurgical and Materials Transactions A 37 (1) (2006) 147–161.
- [3] K. Datta, R. Delhez, P. Bronsveld, J. Beyer, H. J. Geijselaers, J. Post,
 A low-temperature study to examine the role of ε-martensite during
 strain-induced transformations in metastable austenitic stainless steels,
 Acta materialia 57 (11) (2009) 3321–3326.
- [4] S. Tavares, D. Gunderov, V. Stolyarov, J. Neto, Phase transformation
 induced by severe plastic deformation in the aisi 304l stainless steel,
 Materials Science and Engineering: A 358 (1-2) (2003) 32–36.
- ³⁶ [5] J. Venables, The martensite transformation in stainless steel, The Philo-

- sophical Magazine: A Journal of Theoretical Experimental and Applied
 Physics 7 (73) (1962) 35–44.
- [6] P. L. Mangonon, G. Thomas, Structure and properties of thermal mechanically treated 304 stainless steel, Metallurgical transactions 1 (6)
 (1970) 1587–1594.
- [7] G. Olson, M. Cohen, Kinetics of strain-induced martensitic nucleation, Metallurgical transactions A 6 (4) (1975) 791.
- [8] J. Brooks, M. Loretto, R. Smallman, Direct observations of martensite nuclei in stainless steel, Acta Metallurgica 27 (12) (1979) 1839–1847.
- [9] W.-S. Lee, C.-F. Lin, Comparative study of the impact response and microstructure of 304l stainless steel with and without prestrain, Metallurgical and Materials Transactions A 33 (9) (2002) 2801–2810.
- [10] R. B. Figueiredo, F. L. Sicupira, L. R. C. Malheiros, M. Kawasaki, D. B.
 Santos, T. G. Langdon, Formation of epsilon martensite by high-pressure
 torsion in a trip steel, Materials Science and Engineering: A 625 (2015)
 114–118.
- [11] E. Cakmak, S. C. Vogel, H. Choo, Effect of martensitic phase trans formation on the hardening behavior and texture evolution in a 304l
 stainless steel under compression at liquid nitrogen temperature, Materials Science and Engineering: A 589 (2014) 235–241.
- [12] M. Shaira, N. Godin, P. Guy, L. Vanel, J. Courbon, Evaluation of the
 strain-induced martensitic transformation by acoustic emission monitor ing in 304l austenitic stainless steel: Identification of the ae signature

- of the martensitic transformation and power-law statistics, Materials
 Science and Engineering: A 492 (1-2) (2008) 392–399.
- [13] K. Tao, D. W. Brown, S. C. Vogel, H. Choo, Texture evolution during
 strain-induced martensitic phase transformation in 304l stainless steel
 at a cryogenic temperature, Metallurgical and Materials Transactions A
 37 (12) (2006) 3469–3475.
- [14] D. Gu, W. Meiners, K. Wissenbach, R. Poprawe, Laser additive manufacturing of metallic components: materials, processes and mechanisms,
 International materials reviews 57 (3) (2012) 133–164.
- [15] P. Åkerfeldt, M.-L. Antti, R. Pederson, Influence of microstructure on
 mechanical properties of laser metal wire-deposited ti-6al-4v, Materials
 Science and Engineering: A 674 (2016) 428–437.
- [16] D. Brown, D. Adams, L. Balogh, J. Carpenter, B. Clausen, G. King, B. Reedlunn, T. Palmer, M. Maguire, S. Vogel, In situ neutron diffraction study of the influence of microstructure on the mechanical response of additively manufactured 304l stainless steel, Metallurgical and Materials Transactions A 48 (12) (2017) 6055–6069.
- 677 [17] B. E. Carroll, T. A. Palmer, A. M. Beese, Anisotropic tensile behav-678 ior of ti-6al-4v components fabricated with directed energy deposition 679 additive manufacturing, Acta Materialia 87 (2015) 309–320.
- [18] N. C. Ferreri, S. Ghorbanpour, S. Bhowmik, R. Lussier, J. Bicknell, B. M. Patterson, M. Knezevic, Effects of build orientation and heat treatment on the evolution of microstructure and mechanical properties

- of alloy mar-m-509 fabricated via laser powder bed fusion, International
 Journal of Plasticity.
- [19] S. Gribbin, S. Ghorbanpour, N. C. Ferreri, J. Bicknell, I. Tsukrov,
 M. Knezevic, Role of grain structure, grain boundaries, crystallographic
 texture, precipitates, and porosity on fatigue behavior of inconel 718 at
 room and elevated temperatures, Materials Characterization 149 (2019)
 184–197.
- [20] Z. Wang, T. A. Palmer, A. M. Beese, Effect of processing parameters on microstructure and tensile properties of austenitic stainless steel 304l made by directed energy deposition additive manufacturing, Acta Materialia 110 (2016) 226–235.
- [21] S. Gribbin, J. Bicknell, L. Jorgensen, I. Tsukrov, M. Knezevic, Low
 cycle fatigue behavior of direct metal laser sintered inconel alloy 718,
 International Journal of Fatigue 93 (2016) 156–167.
- [22] D. H. Smith, J. Bicknell, L. Jorgensen, B. M. Patterson, N. L. Cordes,
 I. Tsukrov, M. Knezevic, Microstructure and mechanical behavior of
 direct metal laser sintered inconel alloy 718, Materials Characterization
 113 (2016) 1–9.
- [23] D. Brown, J. Almer, B. Clausen, P. Mosbrucker, T. Sisneros, S. Vogel, Twinning and de-twinning in beryllium during strain path changes,
 Materials Science and Engineering: A 559 (2013) 29–39.
- [24] H. Van Swygenhoven, S. Van Petegem, In-situ mechanical testing during
 x-ray diffraction, Materials Characterization 78 (2013) 47–59.

- [25] P. E. Vullum, J. Mastin, J. Wright, M.-A. Einarsrud, R. Holmestad,
 T. Grande, In situ synchrotron x-ray diffraction of ferroelastic la0. 8ca0.
 2coo3 ceramics during uniaxial compression, Acta materialia 54 (10)
 (2006) 2615–2624.
- [26] C. A. Bronkhorst, J. R. Mayeur, V. Livescu, R. Pokharel, D. W. Brown,
 G. T. Gray III, Structural representation of additively manufactured
 316l austenitic stainless steel, International Journal of Plasticity 118
 (2019) 70–86.
- [27] R. Pokharel, A. Patra, D. W. Brown, B. Clausen, S. C. Vogel, G. T.
 Gray III, An analysis of phase stresses in additively manufactured 304l
 stainless steel using neutron diffraction measurements and crystal plasticity finite element simulations, International Journal of Plasticity.
- [28] M. Zecevic, Y. P. Korkolis, T. Kuwabara, M. Knezevic, Dual-phase steel
 sheets under cyclic tension–compression to large strains: experiments
 and crystal plasticity modeling, Journal of the Mechanics and Physics
 of Solids 96 (2016) 65–87.
- 722 [29] A. M. Cantara, M. Zecevic, A. Eghtesad, C. M. Poulin, M. Kneze-723 vic, Predicting elastic anisotropy of dual-phase steels based on crystal 724 mechanics and microstructure, International Journal of Mechanical Sci-725 ences 151 (2019) 639–649.
- [30] M. Zecevic, M. V. Upadhyay, E. Polatidis, T. Panzner, H. Van Swygenhoven, M. Knezevic, A crystallographic extension to the olson-cohen

- model for predicting strain path dependence of martensitic transformation, Acta Materialia 166 (2019) 386–401.
- 730 [31] D. Brown, D. Adams, L. Balogh, J. Carpenter, B. Clausen, V. Livescu,
 R. Martinez, B. Morrow, T. Palmer, R. Pokharel, et al., Using in situ
 neutron diffraction to isolate specific features of additively manufactured microstructures in 304l stainless steel and identify their effects on
 macroscopic strength, Metallurgical and Materials Transactions A 50 (7)
 (2019) 3399–3413.
- [32] G. T. Gray, V. Livescu, P. Rigg, C. P. Trujillo, C. M. Cady, S.-R. Chen,
 J. S. Carpenter, T. J. Lienert, S. J. Fensin, C. M. Knapp, et al., L2 mile stone 5433: Characterization of dynamic behavior of am and conventionally processed stainless steel (316l and 304l), Tech. rep., Los Alamos
 National Lab.(LANL), Los Alamos, NM (United States) (2016).
- [33] B. M. Morrow, T. J. Lienert, C. M. Knapp, J. O. Sutton, M. J. Brand,
 R. M. Pacheco, V. Livescu, J. S. Carpenter, G. T. Gray, Impact of
 defects in powder feedstock materials on microstructure of 304l and 316l
 stainless steel produced by additive manufacturing, Metallurgical and
 Materials Transactions A 49 (8) (2018) 3637–3650.
- [34] R. Pokharel, L. Balogh, D. Brown, B. Clausen, G. Gray III, V. Livescu,
 S. Vogel, S. Takajo, Signatures of the unique microstructure of additively manufactured steel observed via diffraction, Scripta Materialia
 155 (2018) 16–20.

- [35] E. O. S, Eos stainlesssteel ph 1. materials data sheet 6. available from:.

 URL https://www.eos.info/material-m
- 752 [36] N.I.S.T., Reference material 674b x-ray powder diffraction intensity set 753 for quantitative analysis by x-ray powder diffraction. (2007).
- [37] B. H. Toby, R. B. Von Dreele, Gsas-ii: the genesis of a modern opensource all purpose crystallography software package, Journal of Applied Crystallography 46 (2) (2013) 544–549.
- The use of high energy x-rays from the advanced photon source to study stresses in materials, Materials Science and Engineering: A 399 (1-2) (2005) 120–127.
- [39] D. Mainprice, F. Bachmann, R. Hielscher, H. Schaeben, Descriptive
 tools for the analysis of texture projects with large datasets using mtex:
 strength, symmetry and components, Geological Society, London, Special Publications 409 (1) (2015) 251–271.
- [40] S. I. Wright, M. M. Nowell, S. P. Lindeman, P. P. Camus, M. De Graef,
 M. A. Jackson, Introduction and comparison of new ebsd post-processing
 methodologies, Ultramicroscopy 159 (2015) 81–94.
- [41] R. A. Young, The rietveld method, Vol. 5, International union of crystallography, 1993.
- [42] L.-M. Peng, G. Ren, S. Dudarev, M. Whelan, Debye–waller factors and
 absorptive scattering factors of elemental crystals, Acta Crystallographical
 ica Section A: Foundations of Crystallography 52 (3) (1996) 456–470.

- ⁷⁷² [43] E. Purushotham, N. G. Krishna, X-ray determination of crystallite size ⁷⁷³ and effect of lattice strain on debye–waller factors of platinum nano ⁷⁷⁴ powders, Bulletin of Materials Science 36 (6) (2013) 973–976.
- Y. Zhong, F. Yin, T. Sakaguchi, K. Nagai, K. Yang, Dislocation structure evolution and characterization in the compression deformed mn–cu alloy, Acta materialia 55 (8) (2007) 2747–2756.
- ⁷⁷⁸ [45] G. E. Dieter, H. A. Kuhn, S. L. Semiatin, Handbook of workability and process design, ASM international, 2003.
- [46] J.-H. Jun, C.-S. Choi, Variation of stacking fault energy with austenite grain size and its effect on the ms temperature of $\gamma \to \epsilon$ martensitic transformation in fe–mn alloy, Materials Science and Engineering: A 257 (2) (1998) 353–356.
- ⁷⁸⁴ [47] M. Hatherly, A. Malin, Deformation of copper and low stacking-fault energy, copperbase alloys, Metals Technology 6 (1) (1979) 308–319.
- [48] S. W. Cheong, H. Weiland, Understanding a microstructure using gos
 (grain orientation spread) and its application to recrystallization study
 of hot deformed al-cu-mg alloys, in: Materials Science Forum, Vol. 558,
 Trans Tech Publ, 2007, pp. 153–158.
- ⁷⁹⁰ [49] Z. Nishiyama, Martensitic transformation, Elsevier, 2012.
- [50] S. Pisarik, D. Van Aken, Crystallographic orientation of the $\epsilon \to \alpha'$ martensitic (athermal) transformation in a femnalsi steel, Metallurgical and Materials Transactions A 45 (8) (2014) 3173–3178.

- [51] E. Oliver, P. Withers, M. Daymond, S. Ueta, T. Mori, Neutron-diffraction study of stress-induced martensitic transformation in trip
 steel, Applied Physics A 74 (1) (2002) s1143-s1145.
- ⁷⁹⁷ [52] R. E. Smallman, Modern physical metallurgy, Elsevier, 2016.
- ⁷⁹⁸ [53] N. Hansen, Hall–petch relation and boundary strengthening, Scripta
 ⁷⁹⁹ Materialia 51 (8) (2004) 801–806.
- [54] Y. Kok, X. P. Tan, P. Wang, M. Nai, N. H. Loh, E. Liu, S. B. Tor,
 Anisotropy and heterogeneity of microstructure and mechanical properties in metal additive manufacturing: A critical review, Materials & Design 139 (2018) 565–586.
- [55] R. Schramm, R. Reed, Stacking fault energies of seven commercial
 austenitic stainless steels, Metallurgical Transactions A 6 (7) (1975)
 1345.
- [56] H.-R. Wenk, L. Lutterotti, S. Vogel, Texture analysis with the new
 hippo tof diffractometer, Nuclear Instruments and Methods in Physics
 Research Section A: Accelerators, Spectrometers, Detectors and Associated Equipment 515 (3) (2003) 575–588.

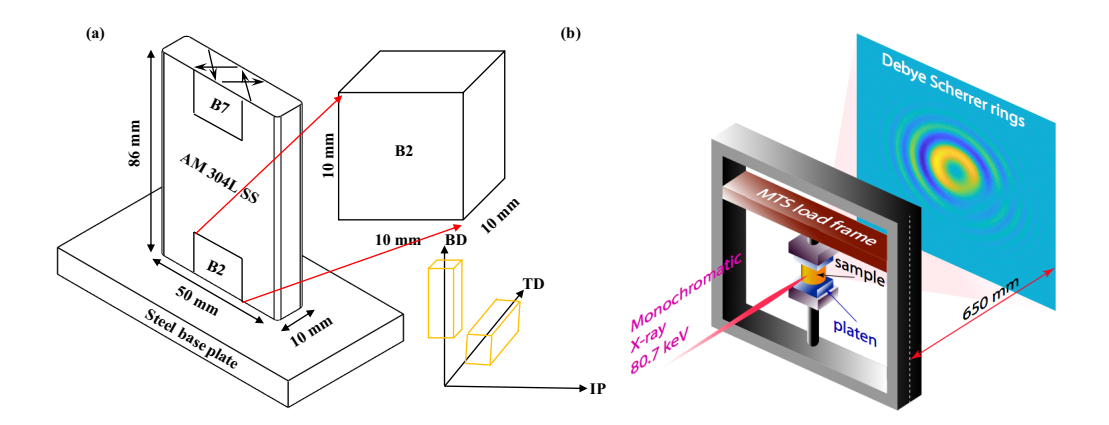


Figure 1: (a) Build geometries of the AM-304L-SS plate and regions/blocks within the plate (B2 and B7) from which compression samples were excised. Arrows on top of the AM-304L-SS plate indicate rotation (67.5°) of the laser path every after every pass. Sample orientation with respect to build frame is indicated where BD is the build direction, TD is the through-thickness direction, and IP is the in-plane direction. (b) Schematic of the experimental apparatus for X-ray diffraction measurements during in situ compressive loading. MTS servo-hydraulic load frame was used, where the sample was held between two die, which exert a compressive force on the sample while allowing unobstructed path for the incident high-energy monochromatic X-rays and outgoing diffracted X-rays.

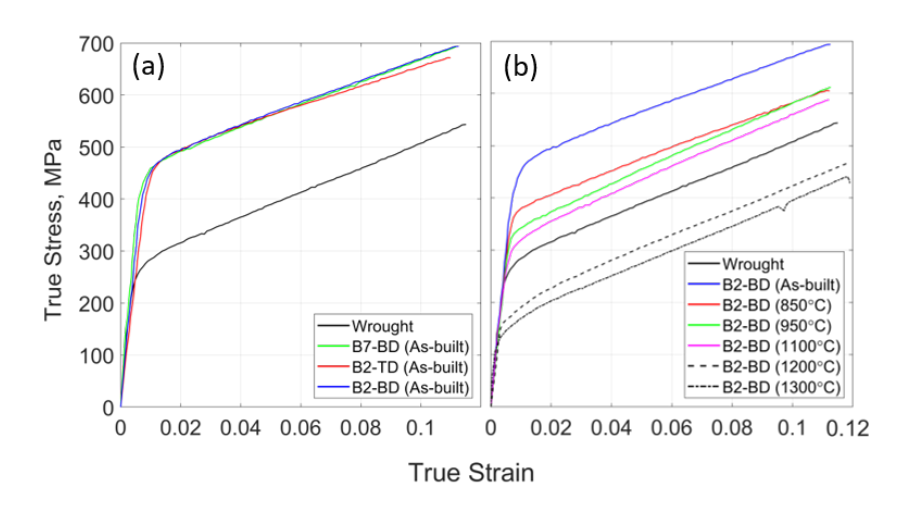


Figure 2: True stress-strain behavior of wrought and AM-304L-SS in simple compression. AM samples were oriented with BD or TD parallel to the loading axis during compression and were cut from one of two different regions (B2 or B7) on an AM plate (a). AM samples underwent one (or none) of several heat-treatments prior to loading, were oriented with BD parallel to the loading axis during compression and were cut from the B2 region on the initial AM plate (b).

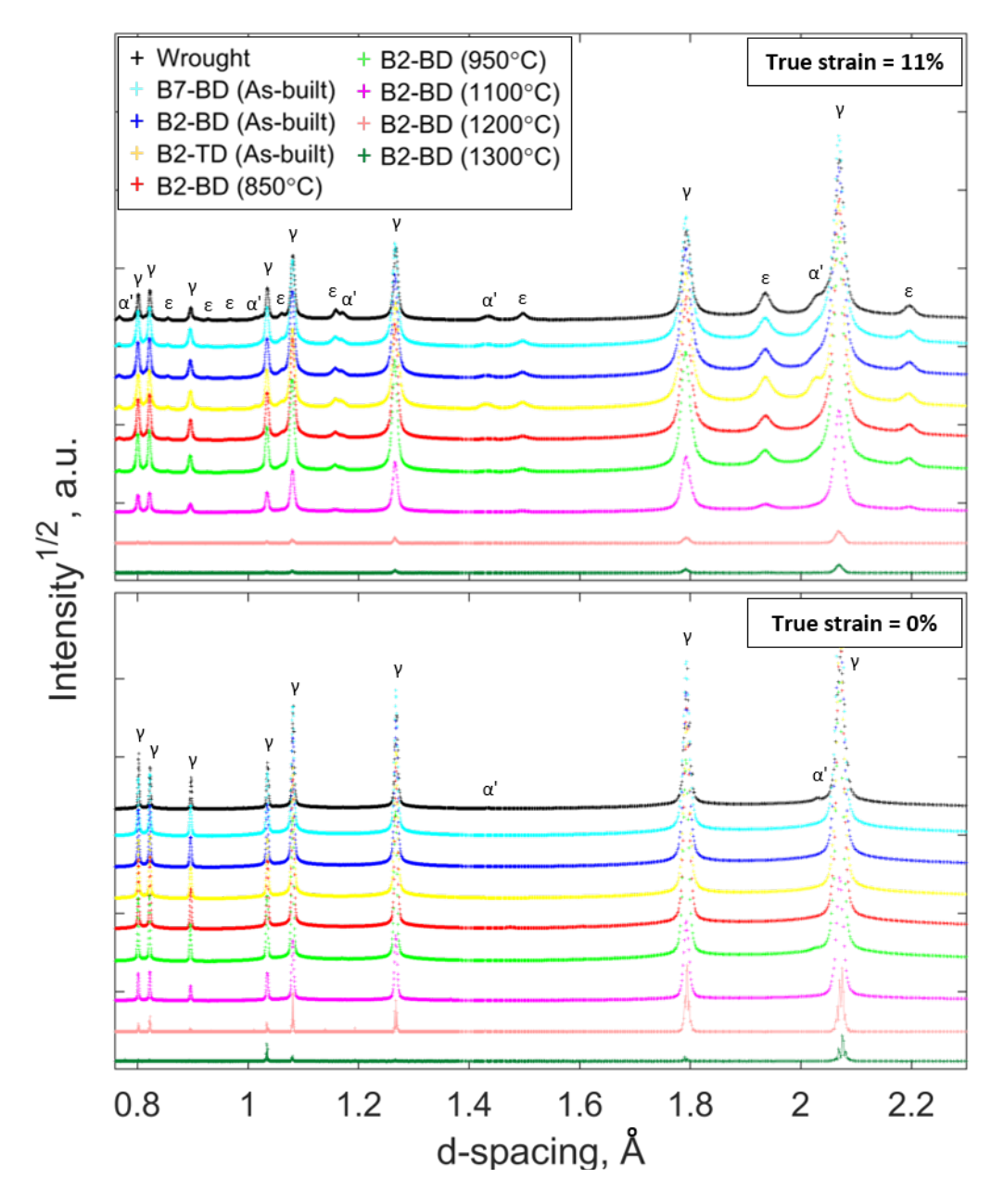


Figure 3: Diffraction profile created from single exposures prior to (true strain = 0%) and during (true strain = 11%) in situ loading of wrought, as-built AM, and heat-treated AM 304L stainless steel samples. Bragg reflections for austenite (γ), α' martensite, and ϵ martensite phases are also indicated. Y-axis units are arbitrary (a.u.).

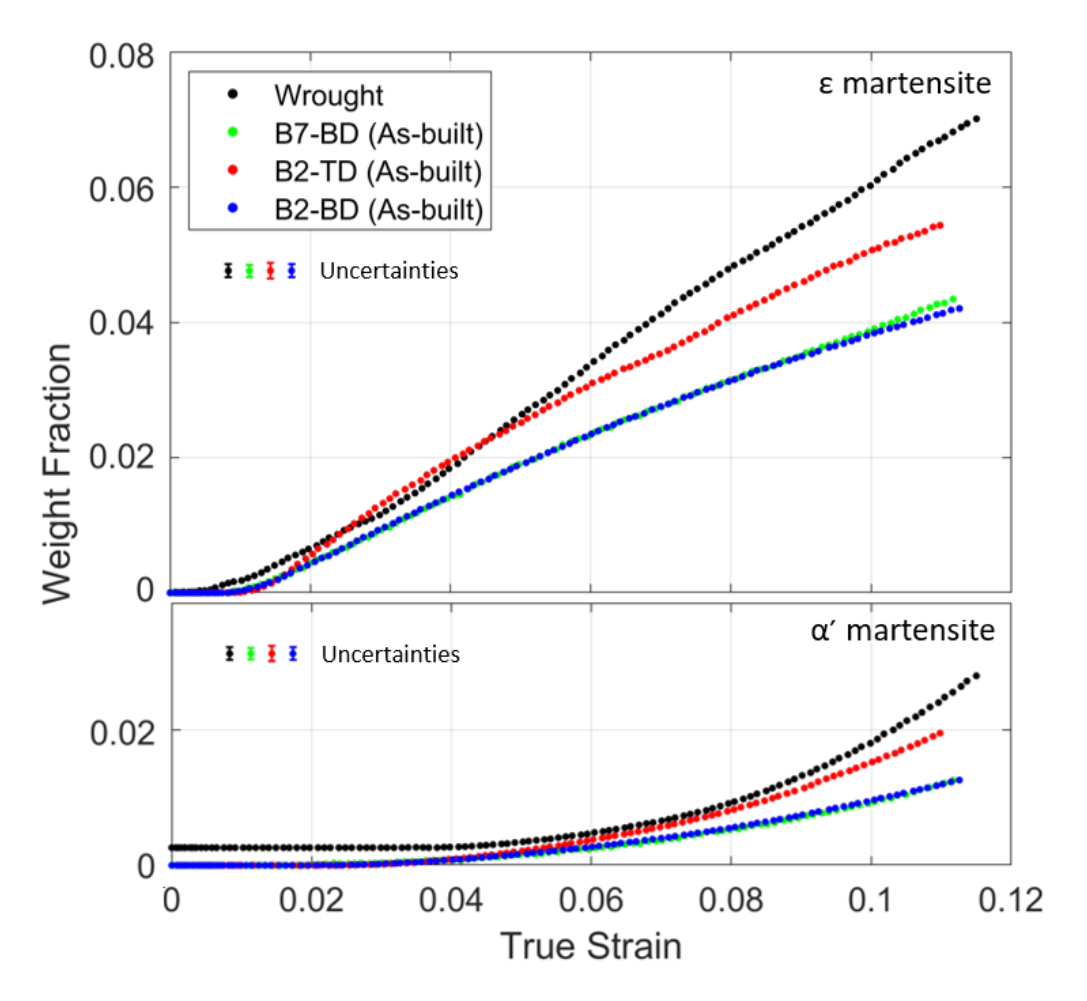


Figure 4: Evolution of ϵ and α' martensite in wrought and AM-304L-SS during monotonic compression as determined by *in situ* x-ray diffraction. AM samples were oriented with BD or TD parallel to the loading axis during compression and were cut from one of two different regions on an AM plate (B2, B7). The error bars below the legend indicate the average uncertainty in each dataset.

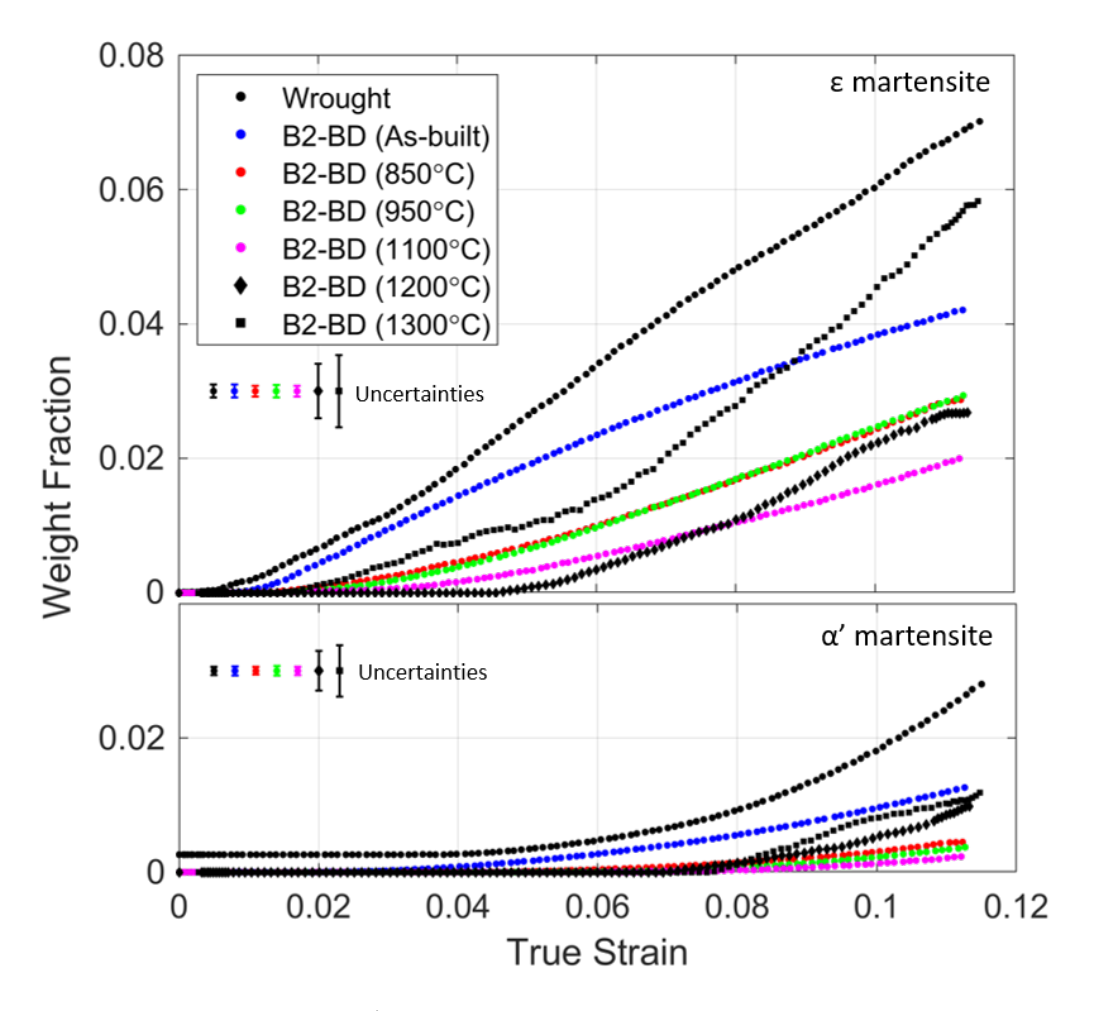


Figure 5: Evolution of ϵ and α' martensite in wrought, as-built-AM and heat-treated-AM 304L-SS during monotonic compression as determined by $in\ situ$ x-ray diffraction. AM samples underwent one (or none) of several heat-treatments prior to loading. The error bars below the legend indicate the average uncertainty in each dataset.

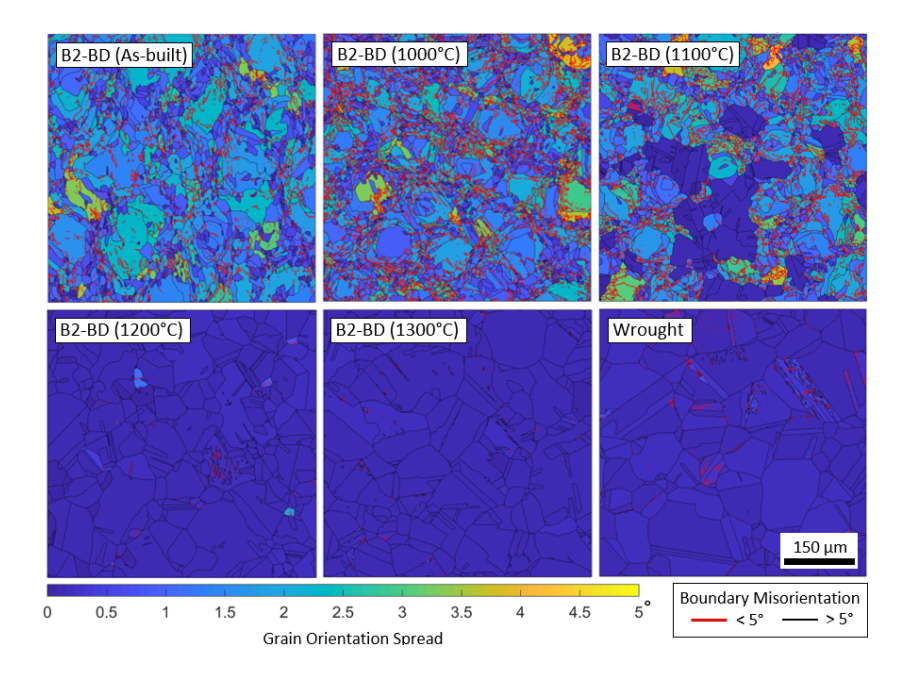


Figure 6: Grain orientation spread (GOS) maps created from EBSD data for undeformed wrought and AM (as-built and heat-treated) 304L-SS samples. Black lines highlight grain boundaries and red lines highlight sub-grain boundaries. All maps have 500 μ m view fields, and the axis perpendicular to the maps for the AM sample is BD.

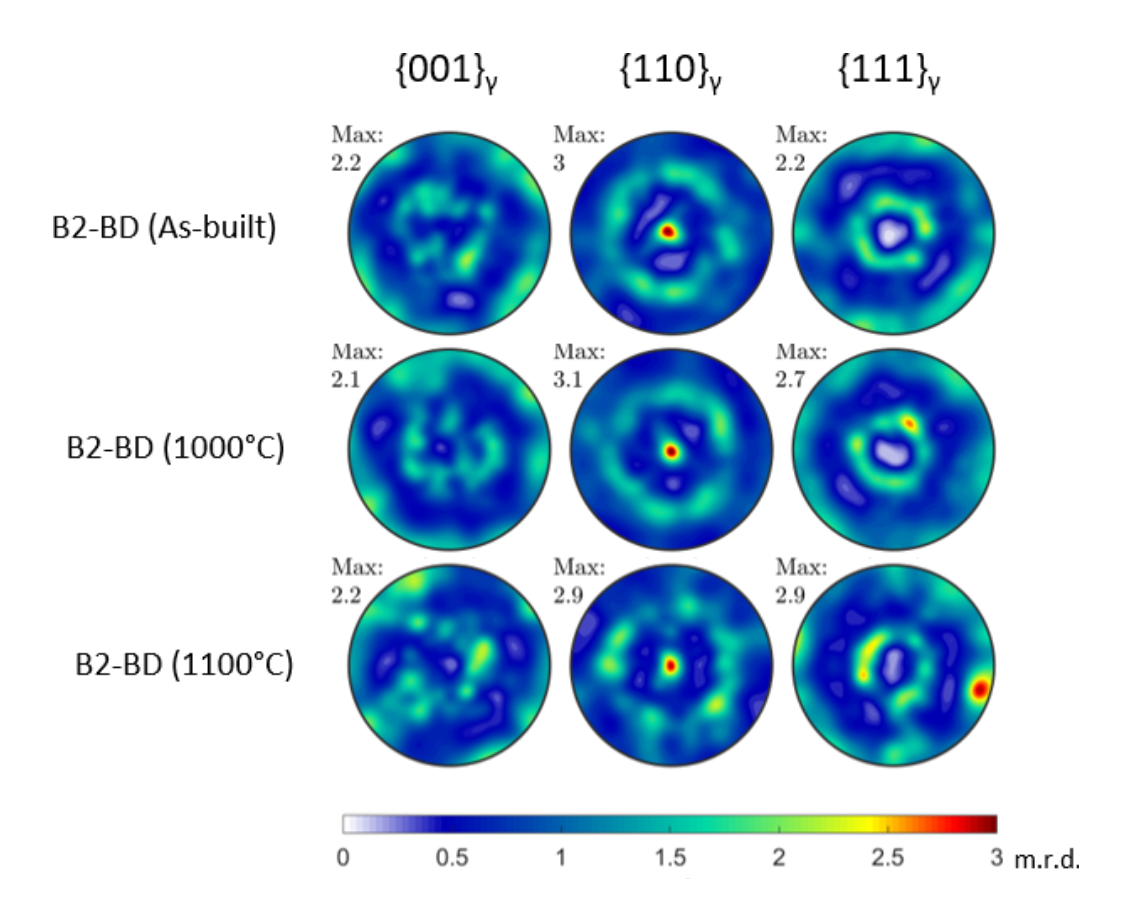


Figure 7: Pole figures created from EBSD data which show austenite texture for selected AM (as-built and heat-treated) 304L-SS samples. BD is out of plane for all pole figures. Intensities are measured in multiples of random distribution (m.r.d.).

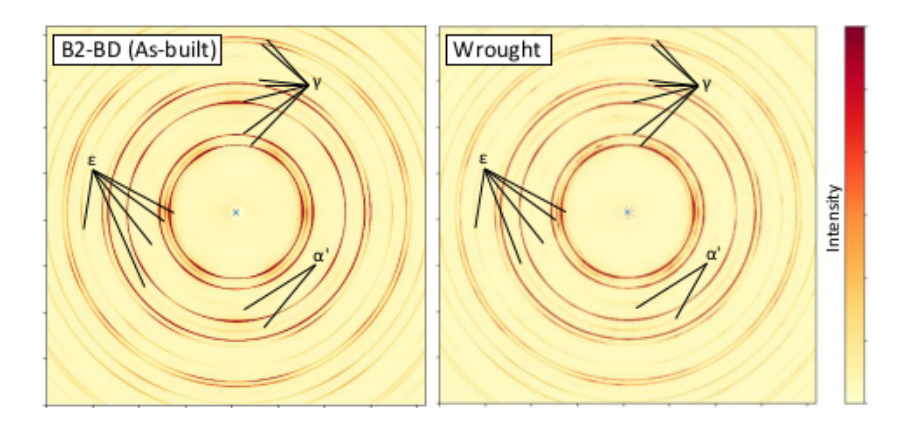


Figure 8: Raw detector images of the as-built (left) and the wrought (right) 304L-SS after 11% compressive strain.

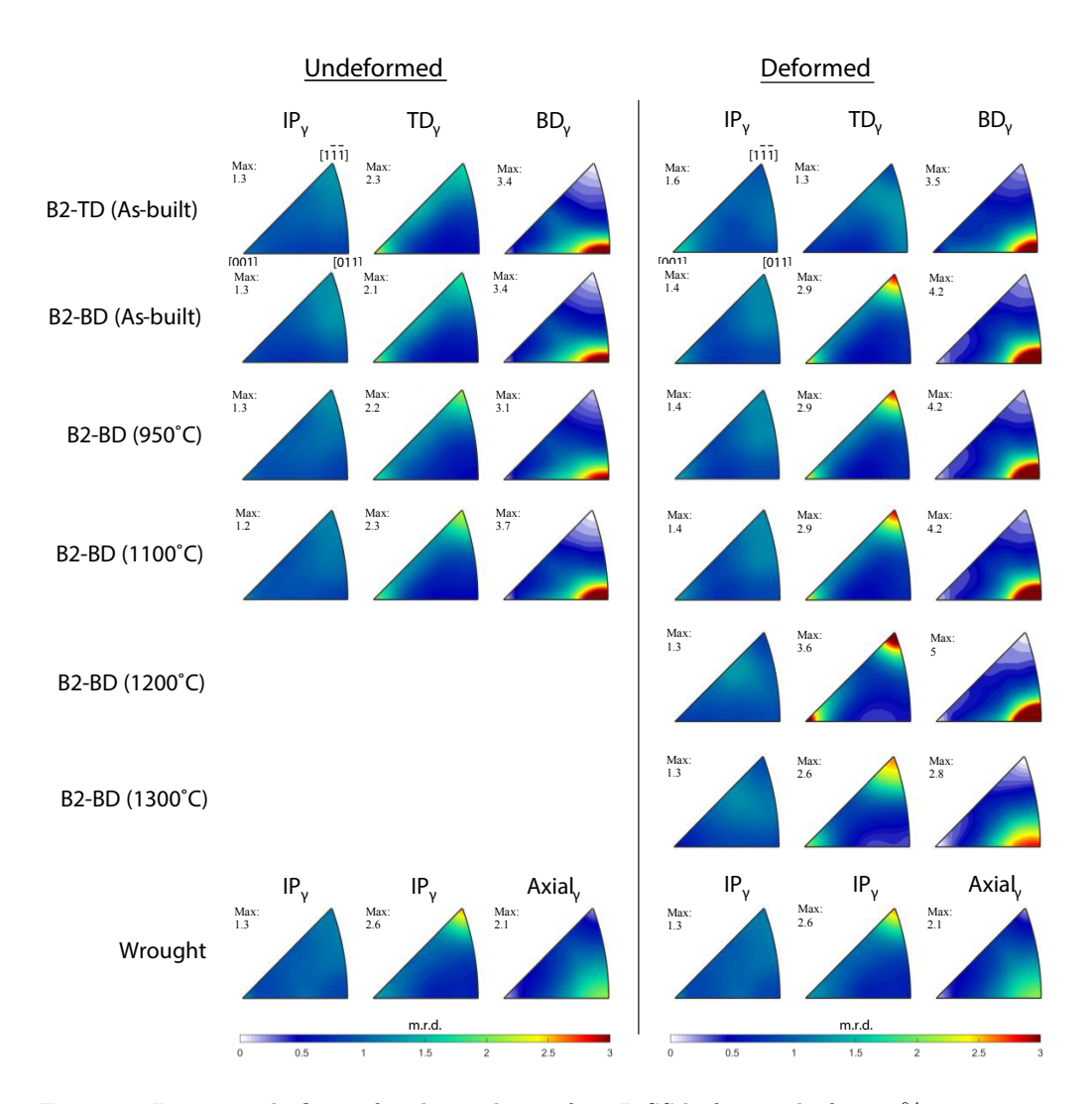


Figure 9: Inverse pole figure for the γ phase of 304L-SS before and after 11% compressive strain.

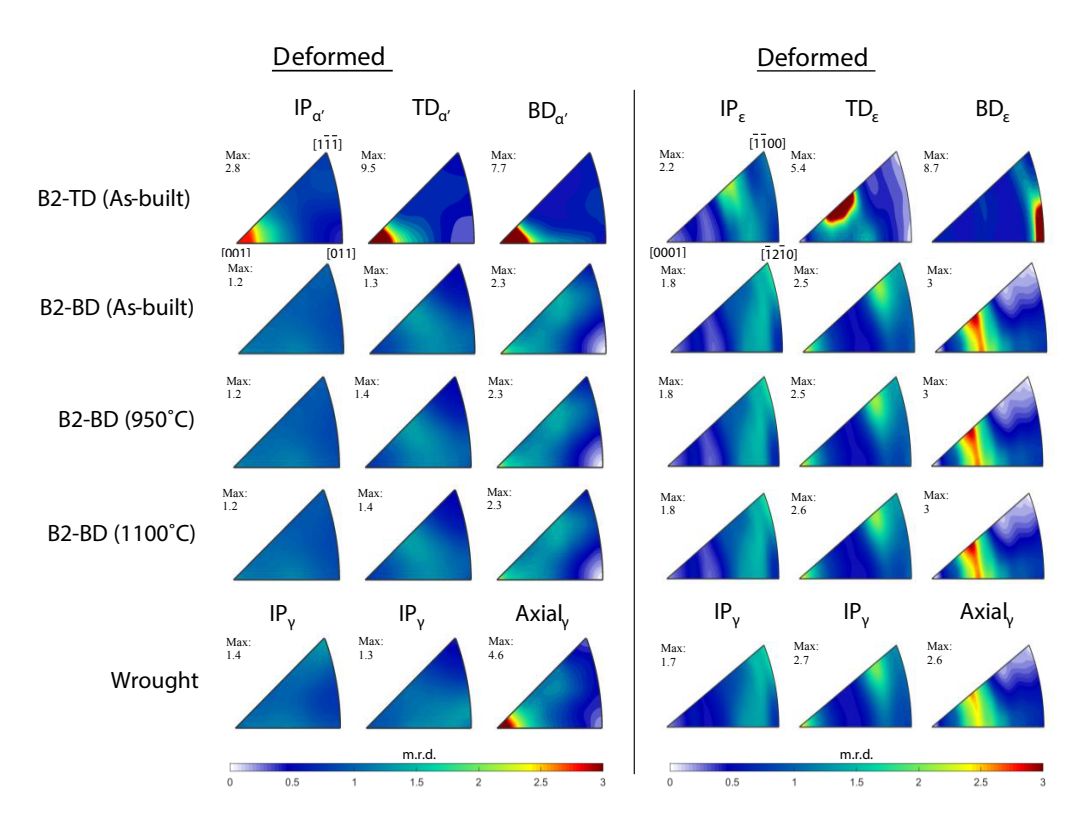


Figure 10: Inverse pole figure for α '(left) and ϵ (right) phases of 304L-SS before and after 11% compressive strain.

Table 1: The initial and final (true strain = 11%) martensite phase compositions as a result of *in situ* compressive loading of wrought and two AM 304L stainless steels. AM samples were oriented with BD parallel or normal (TD) to the loading axis during compression and were cut from one of two different regions on an AM plate (B2, B7). The units are in wt. %. Final phase value is a product of profile fitting uncertainty in GSAS-II, given in parenthesis. Note the phase compositions add to 100% with austenite as balance.

	$\epsilon_{initial}$	ϵ_{final}	$\alpha_{initial}$	α_{final} ,
Wrought	0.0	7.01 (0.10)	0.26	2.80 (0.06)
B2-BD (As-built)	0.0	4.21(0.10)	0.0	1.26 (0.07)
B2-TD (As-built)	0.0	5.44(0.12)	0.0	1.95(0.08)
B7-BD (As-built)	0.0	4.34 (0.09)	0.0	$1.25 \ (0.06)$

Table 2: Initial and final (true strain = 11%) martensite phase compositions as a result of in situ compressive loading of wrought and AM (as-built and heat-treated) 304L stainless steel. The units are in wt. %. Final phase value is a product of profile fitting uncertainty in GSAS-II, given in parenthesis. Note the phase compositions add to 100% with austenite as balance.

	$\epsilon_{initial}$	ϵ_{final}	$\alpha_{initial}$	α_{final} ,
Wrought	0.0	7.01 (0.10)	0.26	2.80 (0.06)
B2-BD (As-built)	0.0	4.21 (0.10)	0.0	1.26 (0.07)
B2-BD (850°)	0.0	2.87 (0.09)	0.0	0.45 (0.06)
B2-BD (950°)	0.0	2.94(0.10)	0.0	0.37 (0.07)
B2-BD (1100°)	0.0	2.00(0.09)	0.0	0.23 (0.06)
B2-BD (1200°)	0.0	2.68 (0.43)	0.0	0.98(0.31)
B2-BD (1300°)	0.0	5.83 (0.55)	0.0	1.18 (0.40)

Table 3: Mean kernel average misorientation (KAM), mean grain orientation spread (GOS) and mean crystallite size for undeformed wrought and AM (as-built and heat-treated) 304L stainless steels. EBSD data was used to reconstruct sample microstructures from which these values were calculated. Standard deviation assuming normal distribution is expressed in brackets.

	<kam> [°]</kam>	$\langle GOS \rangle [^{\circ}]$	$<$ Crystallite size $>$ [μ m]
Wrought	0.31 [0.15]	0.32 [0.10]	63.0 [31.4]
B2-BD (As-built)	0.56 [0.53]	3.11 [1.43]	23.5 [19.8]
B2-BD (1000°)	0.74 [0.69]	3.12[1.49]	16.1 [14.3]
B2-BD (1100°)	0.63 [0.66]	2.75 [1.89]	21.0 [17.4]
B2-BD (1200°)	0.22 [0.10]	0.26 [0.17]	50.1 [26.6]
B2-BD (1300°)	0.22 [0.09]	0.24 [0.05]	57.7 [29.3]